PROCEEDINGS OF SCIENCE

New insights into the nucleon's electromagnetic structure

Hans-Werner Hammer[a,b,*]

[a] *Technische Universität Darmstadt, Department of Physics, 64289 Darmstadt, Germany*

[b] *GSI Helmholtzzentrum für Schwerionenforschung GmbH, ExtreMe Matter Institute EMMI and Helmholtz Forschungsakademie Hessen für FAIR (HFHF), 64291 Darmstadt, Germany*

E-mail: `hans-werner.hammer@physik.tu-darmstadt.de`

We present a combined analysis of the electromagnetic form factors of the nucleon in the space- and time-like regions using dispersion theory. Our framework provides a consistent description of the experimental data over the full range of momentum transfer, in line with the constraints from analyticity and unitarity. The statistical uncertainties of the extracted form factors are estimated using the bootstrap method, while systematic errors are determined from variations of the spectral functions. From the form factors, we determine precise values for the nucleon radii and comment on their puzzling status.

The 11th International Workshop on Chiral Dynamics (CD2024)
26-30 August 2024
Ruhr University Bochum, Germany

---

[*] Speaker

1. Introduction

The electromagnetic (EM) structure of the nucleon is described by its EM form factors. They provide a window on the strong interaction dynamics in the nucleon responsible for the EM structure from large to small distances. At small momentum transfers, they probe the large-distance properties of the nucleon like the charge and magnetic moment, while the quark substructure of the nucleon determines the behavior at large momentum transfer. For recent reviews see, e.g., Refs. [1–4]. The fundamental role of the EM form factors is underscored by their importance for the description of physical quantities ranging from the Lamb shift in atomic physics [5–8] over the strangeness content of the nucleon [9, 10] in hadron physics to the EM structure and reactions of atomic nuclei [11, 12].

The EM nucleon form factors and radii are determined by the matrix element of the electromagnetic current $j_\mu^{\rm EM}(x)$ in the nucleon. Denoting a nucleon state with four-momentum p as $|N(p)\rangle$, this matrix element can be written as

$$\langle N(p')|j_\mu^{\rm EM}(0)|N(p)\rangle = \bar{u}(p')\left[F_1(t)\gamma_\mu + i\frac{F_2(t)}{2m}\sigma_{\mu\nu}q^\nu\right]u(p)\,, \tag{1}$$

where m is the nucleon mass and $t = (p' - p)^2$ the four-momentum transfer squared (spin indices have been suppressed). The scalar functions $F_1(t)$ and $F_2(t)$ are the Dirac and Pauli form factors of the nucleon, respectively. Their normalization at $t = 0$ is determined by the charges and anomalous magnetic moments of the nucleon, $F_1^p(0) = 1$, $F_1^n(0) = 0$, $F_2^p(0) = \kappa_p$, $F_2^n(0) = \kappa_n$, with $\kappa_p = 1.793$ and $\kappa_n = -1.913$ in units of the nuclear magneton, $\mu_N = e/(2m)$.

For the theoretical analysis, it is convenient to work in the isospin basis and to decompose the form factors into isoscalar (s) and isovector (v) parts, $F_i^{s/v} = (F_i^p \pm F_i^n)/2$, with $i = 1, 2$. The experimental data are usually given in terms of the Sachs form factors,

$$G_E(t) = F_1(t) - \tau F_2(t)\,, \quad G_M(t) = F_1(t) + F_2(t)\,, \quad \text{where} \quad \tau = -t/(4m^2)\,, \tag{2}$$

which implies $G_E(4m^2) = G_M(4m^2)$.

The nucleon root mean square radii (loosely called radii), $r \equiv \sqrt{\langle r^2\rangle}$, are *defined* via the expansion of the form factors around zero momentum transfer,

$$F(t)/F(0) = 1 + t\langle r^2\rangle/6 + \ldots\,, \tag{3}$$

where $F(t)$ is a generic form factor. In the case of the electric and Dirac form factors of the neutron, G_E^n and F_1^n, the expansion starts with the term linear in t and the normalization factor $F(0)$ is dropped. In the space-like momentum transfer region, $t < 0$, the form factors are real valued quantities. Here it is convenient to use the positive variable $Q^2 = -t$. In the time-like region, $t > 0$, the form factors are complex valued above the two-pion threshold at $t = 4M_\pi^2$.

In Fig. 1, we show the moduli of the form factors $G_E^p(t)$ and $G_E^n(t)$ from the dispersion-theoretical analysis of Ref. [13] to illustrate their behavior. In the space-like region, the physical threshold is located at $t = 0$, whereas the corresponding threshold in the time-like region is $t = 4m^2$. In between these two thresholds, various vector meson poles (plus continua) build up the spectral function to be discussed in detail below. This region cannot be observed.

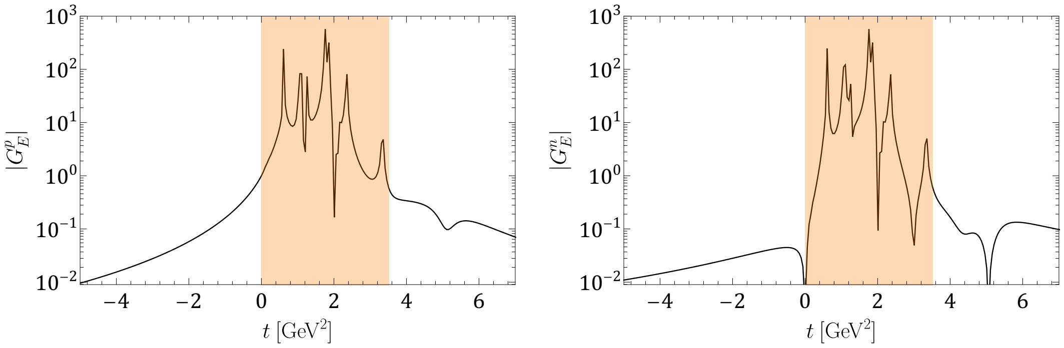

Figure 1: The moduli of electric form factors of the proton, G_E^p, (left panel) and neutron, G_E^n, (right-panel) for space- and time-like momentum transfers from the dispersion-theoretical form factor analysis of Ref. [13]. The colored area extending from $t = 0$ to $t = 4m^2$ along the real axis is the unphysical region where the form factor cannot be observed.

2. Dispersion Relations

Dispersion relations (DRs) provide a powerful tool to extract the form factors from experimental data. Based on the general properties of unitarity and analyticity of a function of complex momentum, they relate the real and imaginary parts of the form factors.

The imaginary part Im F of a form factor F can be constructed from a spectral decomposition [14]. The EM current matrix element in the time-like region ($t > 0$) is given by

$$J_\mu = \langle N(p')\,\bar{N}(\bar{p}')|j_\mu^{\rm EM}(0)|0\rangle = \bar{u}(p')\left[F_1(t)\gamma_\mu + i\frac{F_2(t)}{2m}\sigma_{\mu\nu}(p'+\bar{p}')^\nu\right]v(\bar{p}')\,, \tag{4}$$

where p' and $\bar{p}'$ are the momenta of the nucleon and antinucleon created by the current $j_\mu^{\rm EM}$, respectively, and four-momentum transfer squared is $t = (p' + \bar{p}')^2$.

Using the LSZ reduction formalism, the imaginary part of the form factors is obtained by inserting a complete set of intermediate states [14] as illustrated in Fig. 2,

$$\mathrm{Im}\, J_\mu = \frac{\pi}{Z}(2\pi)^{3/2}\mathcal{N}\sum_n \langle N(p')|\bar{J}_N(0)|n\rangle\langle n|j_\mu^{\rm EM}(0)|0\rangle\, v(\bar{p}')\,\delta^{(4)}(p'+\bar{p}'-p_n)\,, \tag{5}$$

where $\mathcal{N}$ is a nucleon spinor normalization factor, Z is the nucleon wave function renormalization, and $\bar{J}_N(x) = J_N^\dagger(x)\gamma_0$ with $J_N(x)$ a nucleon source. It relates the spectral function to on-shell matrix elements of other processes, as detailed below. Note that the spectral decomposition has to be carried out in the time-like region since the form factors in the space-like region ($t < 0$) are real-valued.

The intermediate states $|n\rangle$ are asymptotic (observable) states of total four-momentum p_n. They carry the *same* quantum numbers as the current $j_\mu^{\rm EM}$:

$$\begin{aligned} I^G(J^{PC}) &= 0^-(1^{--}) \qquad \text{for the isoscalar component}\,, \\ I^G(J^{PC}) &= 1^+(1^{--}) \qquad \text{for the isovector component}\,, \end{aligned} \tag{6}$$

of $j_\mu^{\rm EM}$. Here, I and J denote the isospin $I = 0, 1$ and the angular momentum $J = 1$ of the photon, whereas G, P and C give the G-parity, parity and charge conjugation quantum numbers, respectively.

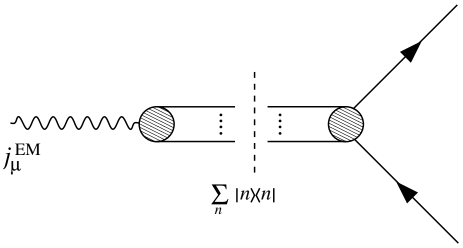

Figure 2: Spectral decomposition of the matrix element of the electromagnetic current $j_\mu^{\rm EM}$ in the nucleon. The intermediate states are denoted $|n\rangle$.

Furthermore, these currents have zero net baryon number. Because of G-parity, states with an odd number of pions only contribute to the isoscalar part, while states with an even number contribute to the isovector part. For the isoscalar part the lowest mass states are: $3\pi, 5\pi, \ldots, K\bar{K}, K\bar{K}\pi, \ldots$, and for the isovector part they are: $2\pi, 4\pi, \ldots K\bar{K}, \ldots$. Associated with each intermediate state is a cut starting at the corresponding threshold in t and running to infinity. As a consequence, the spectral function $\mathrm{Im}\, F(t)$ is different from zero along the cut from t_0 to ∞, with $t_0 = 4\,(9)\, M_\pi^2$ for the isovector (isoscalar) case.

We can use Cauchy's theorem for F with a circular integration contour in the complex t-plane that wraps around the cut for $t \geq t_0$. Assuming the convergence of an unsubtracted dispersion relation, the circular contour can be taken to infinity, and we only pick up the discontinuity of F across the cut. This leads to the dispersion relation

$$F(t) = \lim_{\epsilon \to 0^+} \frac{1}{\pi} \int_{t_0}^{\infty} \frac{\mathrm{Im}\, F(t')}{t' - t - i\epsilon}\, dt' \,, \tag{7}$$

where the $i\epsilon$ defines the integral for values of t on the cut. For proofs of such a representation in perturbation theory, see Ref. [14] (and references therein). One could also use a once-subtracted dispersion relation, since the normalization of the form factors at $t = 0$ is known. However, in what follows, we will only employ the unsubtracted form given in Eq. (7). For the parametrization of the spectral functions described below, the unsubtracted dispersion relations converge by construction.

3. Structure of the spectral functions

The spectral functions are thus the central quantities in the dispersion-theoretical approach. Using Eqs. (4) and (5), they can in principle be reconstructed from experimental data. In practice, however, this program can only be carried out for the lightest two-particle intermediate states.

The longest-range and therefore at low momentum transfer most important continuum contribution comes from the 2π intermediate state which contributes to the isovector form factors [15]. A new precise calculation of this contribution has recently been performed in Ref. [16] including the state-of-the-art pion-nucleon scattering amplitudes from dispersion theory. The resulting spectral functions exhibit the ρ-resonance at $\sqrt{t} = 0.77\,$GeV as well as an enhancement on the left shoulder of the resonance (cf. Fig. 3). This confirms that the ρ is naturally generated as a resonance in $\pi\pi$ scattering [17] and no explicit ρ-meson is required in the isovector spectral function. The enhancement on the left shoulder of the ρ can be traced back to a singularity of the partial wave amplitudes $f_\pm^1(t)$ on the second Riemann sheet [18] (originating from the partial wave projection

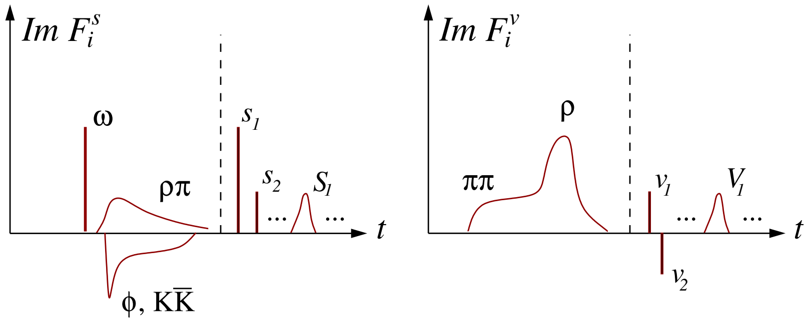

Figure 3: Illustration of the isoscalar (left) and isovector (right) spectral function, showing the continua and (effective) vector meson pole contributions. The vertical dashed line separates the well-constrained low-mass region from the high-mass region which is parameterized by narrow and broad effective poles, indicated by lower and upper case letters, respectively.

of the nucleon pole terms) located at $t_c = 4M_\pi^2 - M_\pi^4/m^2 \approx 3.98\, M_\pi^2$, very close to the physical threshold at $t_0 = 4M_\pi^2$.

The lowest isoscalar continuum is given by three-pion exchange. An analysis based on unitarity alone of this contribution does not exist, but it has been shown in ChPT at leading [19] and subleading [20] orders, that there is no enhancement on the left wing of the ω resonance. Thus, in contrast to the ρ, the inclusion of the ω as a vector meson pole is justified. The first significant continuum contribution to the isoscalar spectral function is due to $K\bar{K}$ and $\rho\pi$ intermediate states. The contributions from the $K\bar{K}$ [21, 22] and $\rho\pi$ [23] were first included in the dispersive analysis of the EM form factors in Ref. [24]. A more detailed discussion of these continua can be found in Ref. [3].

The remaining contributions to the spectral function can be parameterized by vector meson poles. On the one hand, the lower mass poles can be identified with physical vector mesons such as the ω and the ϕ. The higher mass poles on the other hand, are simply an effective way to parameterize higher mass strength in the spectral function. These effective poles at higher momentum transfers appear in both the isoscalar and isovector channels. The (isoscalar and isovector) spectral functions thus take the form

$$\begin{aligned} \operatorname{Im} F_i^s(t) &= \sum_{C=K\bar{K},\rho\pi} \operatorname{Im} F_i^{(s,C)}(t) + \sum_{V=\omega,\phi,s_1,\ldots} \pi a_i^V \delta(M_V^2 - t) + \sum_{V=S_1,\ldots} \operatorname{Im} F_i^{(s,V)}(t)\,, \quad (8) \\ \operatorname{Im} F_i^v(t) &= \operatorname{Im} F_i^{(v,2\pi)}(t) + \sum_{V=v_1,\ldots} \pi a_i^V \delta(M_V^2 - t) + \sum_{V=V_1,\ldots} \operatorname{Im} F_i^{(v,V)}(t)\,, \quad (9) \end{aligned}$$

where $i = 1, 2$ and the broad effective poles are parameterized by a Breit-Wigner form. A cartoon of these spectral functions is shown in Fig. 3. The vertical dashed line separates the phenomenologically well-constrained low-mass region from the effective vector meson poles at higher masses. Here, we allow a variable nonzero width for certain effective poles to mimic the imaginary part of the form factors in the higher-t time-like region, as was done in Ref. [24]. The masses of all effective poles and the widths of the broad poles are fitted to the data. Moreover, all vector meson coupling constants are fitted.

The number of parameters in the spectral function is reduced by enforcing various constraints. The first set of constraints concerns the low-t behavior of the form factors. We enforce the correct normalization of the form factors. The nucleon radii, however, are not included as a constraint. The squared neutron charge radius is an exception. It was constrained to the value from low-energy neutron-atom scattering experiments [25] in previous analyses. In the fits discussed below, we implement this constraint using the high-precision determination of the neutron charge radius squared based on a chiral effective field theory analysis of electron-deuteron scattering [26]: $\langle r_n^2\rangle = -0.105^{+0.005}_{-0.006}$ fm^2 . Extracting the neutron charge radius from the form factor fit leads to consistent results.

Another set of constraints arises at large momentum transfers. Perturbative QCD constrains the behavior of the nucleon electromagnetic form factors for large momentum transfer. The behavior for $Q^2 \to \infty$ is [27]

$$F_i(Q^2) \to Q^{-2(i+1)} \left[\ln\left(Q^2/\Lambda^2_{\rm QCD}\right)\right]^{-\gamma} , \quad i = 1, 2 , \tag{10}$$

where $\gamma = 2 + 4/(3\beta)$ is an anomalous dimension and $\beta = 11 - 2N_f/3$ the leading order QCD β-function. The anomalous dimension $\gamma \approx 2$ depends weakly on the number of flavors, N_f. The power behavior of the form factors at large Q^2 can be easily understood from perturbative gluon exchange. In order to distribute the momentum transfer from the virtual photon to all three quarks in the nucleon, at least two massless gluons have to be exchanged. Since each of the gluons has a propagator $\sim 1/Q^2$, the form factor has to fall off as $1/Q^4$. In the case of F_2, there is additional suppression by $1/Q^2$ since a quark spin has to be flipped. Enforcing the power law behavior of the form factors in the dispersion relation, Eq. (7), leads to superconvergence relations of the form

$$\int_{t_0}^{\infty} {\rm Im}\, F_i(t)\, t^n dt = 0 , \quad i = 1, 2 , \tag{11}$$

with $n = 0$ for F_1 and $n = 0, 1$ for F_2. These are employed in the current analysis.

4. Data Analysis and Uncertainties

Next, we briefly describe how the fits of the spectral functions to data are performed and how the statistical and systematic errors can be determined. We begin by noting that the fit of the free parameters in the spectral function corresponds to an analytical continuation of the experimental data. Thus we are effectively dealing with an ill-posed problem [28, 29]. This implies that increasing the number of poles will not improve the description of the data from some point on. The number of effective poles is determined by the stability criterion of [29], that is, we take the minimum number of poles necessary to fit the data. The number of free parameters is then strongly reduced by the various constraints (unitarity, normalizations, superconvergence relations). These constraints can be implemented as what is called "hard constraints" or "soft constraints", respectively. In the former case, one solves a system of algebraic equations relating the various parameters (couplings, masses), thus reducing the number of free parameters in the fit (for an explicit representation, see e.g. [30]). In the latter case, the χ^2 is augmented by a Lagrange multiplier enforcing the corresponding constraints. Both options are viable and have been used.

It is straightforward to enumerate the number of fit parameters, which is given by the couplings and masses of the vector mesons, $N_V = 4 + 3(N_s + N_v) + 4(N_S + N_V)$, with $N_{s/v}(N_{S/V})$ the number of the effective narrow (broad) isoscalar/isovector poles and the 4 represents the ω and ϕ couplings, minus the number of constraints, given by $N_C = 4 + 6 + 1$, referring to the low-t, the high-t constraints and the neutron charge radius squared, respectively. If the latter in not included, $N_C = 10$. Putting pieces together, we have in total $N_F = N_V - N_C = 3(N_s + N_v) + 4(N_S + N_V) - 7$ or $N_F = 3(N_s + N_v) + 4(N_S + N_V) - 6$ fit parameters (including or excluding the $(r_E^n)^2$-constraint).

The quality of the fits is measured by means of two different χ^2 functions, χ_1^2 and χ_2^2, which are defined as

$$\begin{aligned}\chi_1^2 &= \sum_i \sum_k \frac{(n_k C_i - C(t_i, \theta_i, \vec{p}\,))^2}{(\sigma_i + \nu_i)^2} \,, \\ \chi_2^2 &= \sum_{i,j} \sum_k (n_k C_i - C(t_i, \theta_i, \vec{p}\,))[V^{-1}]_{ij}(n_k C_j - C(t_j, \theta_j, \vec{p}\,)) \,, \end{aligned} \tag{12}$$

where the C_i are the experimental data at the kinematical point t_i, θ_i and the $C(t_i, \theta_i, \vec{p}\,)$ are the theoretical values for a given form factor parametrization for the parameter values contained in $\vec{p}$. For total cross sections and form factor data the dependence on the scattering angles θ_i is dropped. Moreover, the n_k are normalization coefficients for the various data sets (labeled by the integer k and only used in the fits to the differential cross section data in the spacelike region), while σ_i and ν_i are their statistical and systematical errors, respectively. The covariance matrix $V_{ij} = \sigma_i \sigma_j \delta_{ij} + \nu_i \nu_j$. χ_2^2 is used for those experimental data where statistical and systematical errors are given separately, otherwise χ_1^2 is adopted. Furthermore, the χ^2 of each data set is normalized by the number of data points in order to weight the various data sets without bias. The *reduced* χ^2 is given by $\chi^2_{\text{red}} = \chi^2/(N_D - N_F)$, with N_D the number of fitted data points and N_F the number of independent fit parameters.

As noted above the various constraints on the form factors can be implemented algebraically (hard constraints) or by modifying the χ^2 (soft constraints). The latter type of constraints are implemented as additive terms to the total χ^2 of the form $\chi^2_{\text{add.}} = p\,[x - \langle x \rangle]^2 \exp\left(p\,[x - \langle x \rangle]^2\right)$, where $\langle x \rangle$ is the desired value and p is a strength parameter, which regulates the steepness of the exponential well and helps to stabilize the fits [24].

We now turn to the estimation of uncertainty. One method to estimate the *statistical* errors is the bootstrap procedure, see e.g. Ref. [31]. One simulates a large number of data sets compared to the number of data points by randomly varying the points in the original set within the given errors assuming their normal distribution. For the radius extraction, e.g., one fits to each of these data sets separately, extracts the radius from each fit, and considers the distribution of these radius values, the so-called bootstrap distribution. The artificial data sets represent many samples. Therefore, this radius distribution emulates the probability distribution from fits to data from many real measurements. The precondition for using this method are independent and identically distributed data points. This is satisfied when the χ^2 does not depend on the sequential order of the data points.

Another statistical tool to estimate the error intervals of our model parameters is the Bayesian approach, see e.g. Ref. [32] and references therein. In contrast to the interpretation of probabilities in the frequentist approach, where the probability is the frequency of an event to occur over a large number of repeated trials, the Bayesian method uses probabilities to express the current state of knowledge about the unknown parameters. The key ingredients in the analysis are the prior distribution, which quantifies what is known about the model parameters prior to data being measured, and the likelihood function, which describes information about the parameters contained in the data. The prior distribution and likelihood can be combined to derive the posterior distribution by means of Bayes' theorem. The posterior distribution of the model parameters given the data contains the total knowledge about the model parameters after the data have been observed. From a Bayesian perspective, any statistical inference of interest can be obtained through an appropriate analysis of the posterior distribution.

The analysis in [3] demonstrated that both bootstrap sampling and Bayesian analysis yield equivalent statistical errors for the form factors and radii. In the following, we will show results from the bootstrap procedure, as it is easier to implement for large data sets with a greater number of fit parameters. The extraction of the *systematic* uncertainties is the most difficult task. Our strategy is similar to what was already done in Ref. [33], namely to vary the number of isoscalar and isovector poles around the values corresponding to the best solution, where the total χ^2 does not change by more than 1%.

5. Nucleon Form Factor Results

We show physics results based on a recent state-of-the-art dispersion theoretical analysis of the world data set [13]. Specifically, we discuss fits that include the differential cross section from the electron-proton elastic scattering, the proton form factor ratio from the polarization transfer experiments and neutron form factor data in the space-like region, as well as the effective form factor for both the proton and neutron, and the proton form factor ratio in the time-like region. The best fit is found to consist of 3 narrow poles in the isoscalar channel (s) and 5 narrow poles in the isovector channel (v) below the nucleon-nucleon threshold and $3s + 3v$ broad poles above the threshold, that is, $N_s = 3$, $N_v = 5$ and $N_S = N_V = 3$. $\chi^2/\text{d.o.f} = 1.223$ is obtained for this best fit with the $(r_E^n)^2$-constraint included. Note that there are 33 additional normalization constants for the MAMI and PRad data in the spacelike region. These are discussed in detail in Ref. [3]. We remark that fits with fixed normalizations lead to comparable results but larger χ^2/dof.

5.1 Spacelike Form Factors

Figure 4 presents the best fit from Ref. [13] compared to experimental data for the ep cross section. The data include measurements from PRad (top left panel) and MAMI (bottom left panel), the proton form factor ratio $\mu_p G_E^p/G_M^p$ from JLab (top right panel), the neutron electric form factor (middle right panel), and the neutron magnetic form factor (bottom right panel) at spacelike momentum transfer. Notably, in the proton case, Ref. [13] fits the ep cross section data for $Q^2 < 1\,\text{GeV}^2$ and the data for the proton form factor ratio $\mu_P G_E^p/G_M^p$ with $Q^2 > 1\,\text{GeV}^2$. As in earlier fits [34, 35], the data for the proton form factor ratio at $Q^2 < 1\,\text{GeV}^2$, which do not participate in the fit, are well described (see the inset in the right top panel in Fig. 4). This points towards consistency between the two-photon corrected cross section data and the ratio data, that are not affected by such corrections.

Moreover, a decreasing behavior of $G_M^n/(\mu_n G_{\text{dip}})$ and $\mu_p G_E^p/G_M^p$ at large $|t|$ in the spacelike region is explicitly enforced in order to get a good description over the full range of momentum transfers. It turns out that a zero crossing of $\mu_p G_E^p/G_M^p$ is disfavored by the combined analysis of space- and timelike data, while some measurements suggest a zero crossing of this ratio around $t \approx -10\ \text{GeV}^2$ [36]. Thus, higher momentum transfer data are required to settle this issue. We

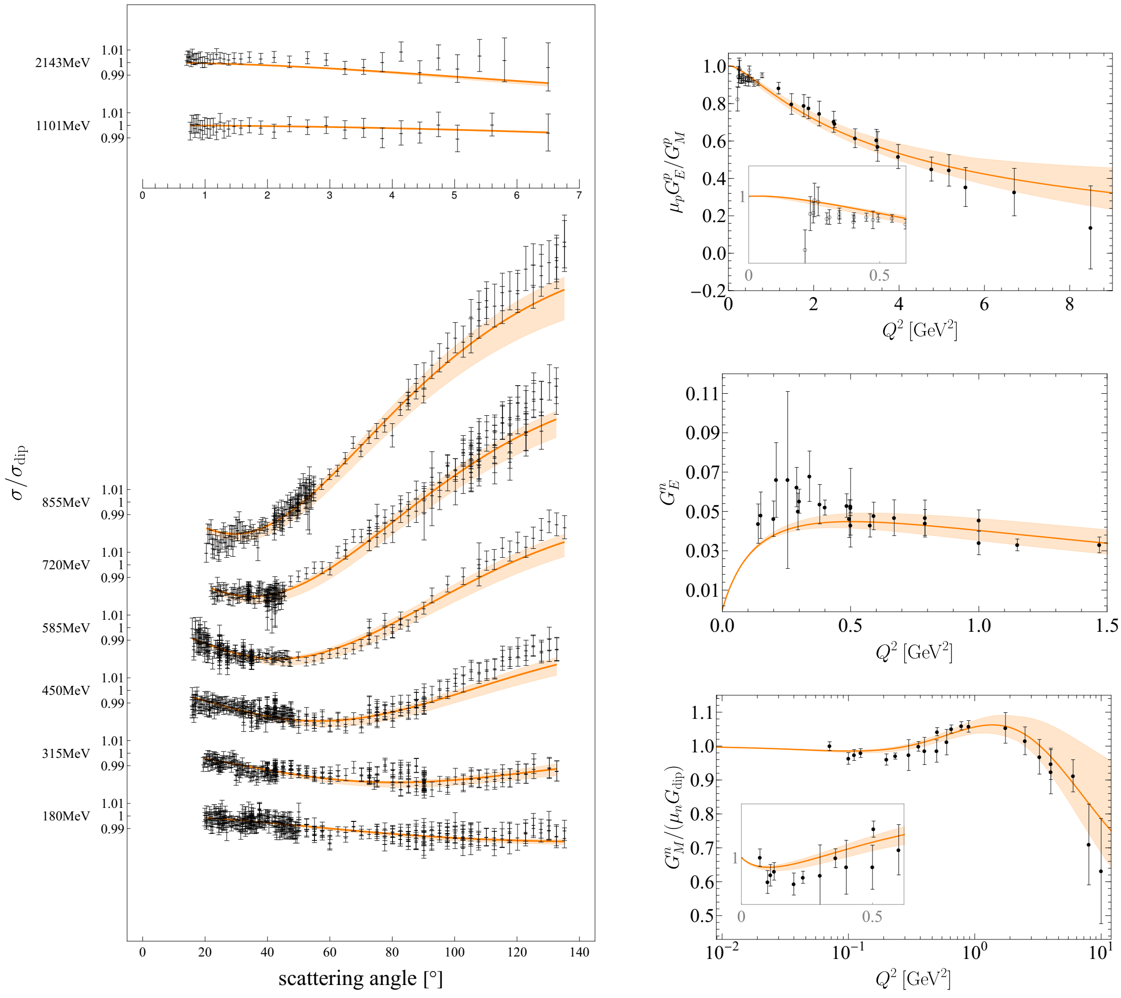

Figure 4: Complete fit to space- and timelike data with bootstrap error (shaded band) compared to the ep cross section data from PRad (left upper panel) and MAMI (left lower panel), the JLab data for $\mu_p G_E^p/G_M^p$ (right top panel), the neutron electric form factor data (right middle panel) and the neutron magnetic form factor data (right bottom panel) at spacelike momentum transfer (see Ref. [13] for explicit references). Fitted data are depicted by closed symbols. The colored bands give the uncertainty due to the bootstrap procedure. Figure taken from Ref. [4].

further remark that as in previous fits to spacelike data only, the onset of perturbative QCD barely sets in at the highest momentum transfers probed.

5.2 Timelike Form Factors

A comparison between the best-fit solution from Ref. [13] and the experimental data for effective form factor

$$|G_{\rm eff}| = \sqrt{(|G_E|^2 + \xi|G_M|^2)/(1+\xi)}\,, \quad \xi = t/(2m^2)\,, \tag{13}$$

of the proton and the neutron is presented in Fig. 5. The fit provides a good description of the

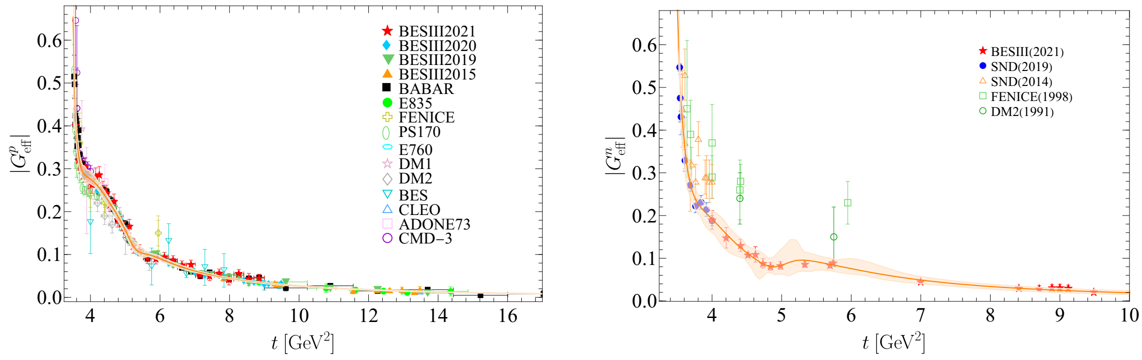

Figure 5: Complete fit to space- and timelike data with bootstrap error (shaded band) compared to data for $|G_{\rm eff}|$ of the proton (left panel) and the neutron (right panel). Fitted data are depicted by closed symbols; data given by open symbols are shown for comparison only (see Ref. [13] for explicit references). Figure taken from Ref. [4].

timelike data for $|G_{\rm eff}|$. With $3s + 5v$ below-threshold narrow poles and $3s + 3v$ above-threshold broad poles, we were able to reproduce both the visible near-threshold enhancement of the proton and the neutron timelike form factors and the prominent oscillations in $|G_{\rm eff}|$ between the threshold at $t = 4m^2$ and $t \approx 6$ GeV^2. In this fit, the observed oscillatory behavior of the nucleon timelike form factors in the intermediate t range arises from the interference among effective vector poles that couple to the nucleon-antinucleon pair, with their masses lying in the corresponding energy range. These poles also generate the imaginary part of the form factors in the physical region. For an alternative viewpoint, see Ref. [37].

5.3 Nucleon Radii

Now we move to the nucleon radii. The radii extracted from the combined fits in [13] are

$$r_E^p = 0.840^{+0.003\,+0.002}_{-0.002\,-0.002}\ \text{fm}, \quad r_M^p = 0.849^{+0.003\,+0.001}_{-0.003\,-0.004}\ \text{fm}, \quad r_M^n = 0.864^{+0.004\,+0.006}_{-0.004\,-0.001}\ \text{fm}, \tag{14}$$

where the first error is statistical (based on the bootstrap procedure) and the second one is systematic (based on the variations in the spectral functions). These values are in good agreement with previous high-precision analyses of spacelike data alone [3, 35] and have comparable errors.

Alternative information on the proton charge radius can be obtained from Lamb shift measurements in electronic as well as muonic hydrogen, see e.g. the reviews [38–40]. The proton radius puzzle—marked by a striking discrepancy between the proton charge radius extracted from muonic hydrogen spectroscopy [5, 41] and the value averaged from electron scattering and ordinary hydrogen spectroscopy [42] has driven extensive experimental efforts in elastic electron-proton scattering over the past decade.

It is remarkable that dispersion-theoretical analyses with the explicit two-pion continuum have always provided a consistent and robust proton charge radius in agreement with the spectroscopic values from muonic hydrogen [5, 41] (cf. the discussion in Ref. [4]. In Fig. 6, we list the most recent experimental determinations of the proton electric radius. Agreement on the proton charge radius has been achieved by the measurements from ep scattering, ep spectroscopy and the μp

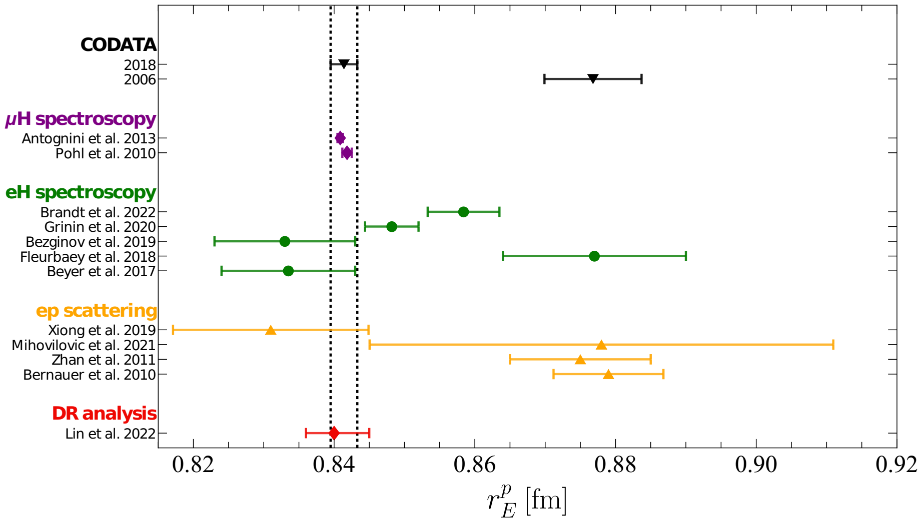

Figure 6: Comparison of the proton charge radius extracted in Ref. [13] and other recent determinations. The y-axis indicates the process in which the proton charge radius was extracted as well as the date and first author of the corresponding work, see Ref. [3] for the relevant references. Figure taken from Ref. [4].

spectroscopy. As a consequence, the value collected in CODATA was updated in 2018 and the 2022 value is 0.84075(64) fm [43] which agrees quite well with the dispersion theoretical determination of Ref. [13]. Moreover, the Zemach radius [44]

$$r_Z = -\frac{4}{\pi}\int_0^\infty \frac{dQ}{Q^2}\left[\frac{G_E(Q^2)G_M(Q^2)}{1+\kappa} - 1\right], \tag{15}$$

and the third Zemach moment $\langle r^3 \rangle_{(2)}$, are obtained as

$$r_z = 1.054^{+0.003\,+0.000}_{-0.002\,-0.001}\ \text{fm}, \quad \langle r^3\rangle_{(2)} = 2.310^{+0.022\,+0.014}_{-0.018\,-0.015}\ \text{fm}^3, \tag{16}$$

in good agreement with Lamb shift and hyperfine splittings in muonic hydrogen [41].

While the electric radius of the proton has attracted much attention in the last decade, this is not true for its magnetic counterpart. The magnetic radius is not probed directly in the Lamb shift in electronic or muonic hydrogen and thus all existing information comes from electron scattering experiments. The ep cross section, however, is dominated by the electric form factor for small momentum transfer. Thus the magnetic radius r_M is more sensitive to larger momentum transfers, and it is not known experimentally with the same precision as r_E. The dispersion-theoretical values of the proton magnetic radius r_M^p were consistently bigger than 0.83 fm and slightly larger than r_E^p. In stark contrast, the analysis of the A1 collaboration [45] yielded a significantly smaller value of $r_M = 0.777(13)_{\text{stat.}}(9)_{\text{syst.}}(5)_{\text{model}}(2)_{\text{group}}$ fm, including in addition to statistical and systematic uncertainties also some uncertainties from the fit model and differences between the two model groups used in the analysis. So is there other information available that could help to clarify this issue? Indeed, lattice QCD calculations at physical pion masses are available. The latest lattice value for r_M given in Ref. [46], $r_M = 0.8111(89)$ fm, roughly corresponds to a 4σ deviation from the dispersive value. Note, however, that the electric radius in that work also comes out rather small, $r_E = 0.820(14)$ fm. The recent results by the PACS collaboration which include finite lattice spacing effects [47] also feature a small magnetic radius, but they have larger errors and are consistent with the dispersive value. These conflicting determinations of the proton magnetic radius appear to present a “new proton radius puzzle" [48]. Assuming that the proton electric radius is known now, a very precise determination of the Zemach radius, Eq. (15), which also enters into the Lamb shift, would give another independent determination of r_M that could help to clarify this issue.

6. Conclusions

These proceedings review the status of the nucleon EM form factors. In particular, we discuss the dispersion-theoretical approach to the EM form factors as well as the radii and highlight recent progress in the field. This approach has become a precision tool to analyze electron scattering and form factor ratio data. We stress that DRs have consistently found a small proton charge radius, $r_E^p \simeq 0.84$ fm, with a slightly larger proton magnetic radius, $r_M^p \simeq 0.85$ fm. Regarding the latter, there are a number of conflicting determinations, which could be regarded as a new “proton radius puzzle". Precise experimental information on the proton magnetic radius is required to sort this out. In the future, the dispersion theoretical analysis should be extended to incorporate the upcoming muon-proton scattering data from the MUSE [49] and AMBER [50] experiments, aiming to definitively resolve the proton radius.

We have also discussed our present understanding of the physics in both the space- and time-like regions. First, the combined analysis of space- and timelike data disfavors a zero crossing for the proton form factor ratio $\mu_p G_E^p/G_M^p$ at spacelike momentum transfer. Second, both the strong near-threshold enhancement and the prominent oscillations in $|G_{\text{eff}}|$ between the two-nucleon threshold and $t \approx 6$ GeV^2 can be described after introducing a certain number of broad poles above threshold in the spectral functions. These poles also generate the imaginary part in the physical region.

For the neutron data basis, a thorough analysis of the existing electron-deuteron and electron-^{3}He scattering data based on chiral effective field theory and including two-photon corrections should be performed. This would allow to consistently analyze the proton and neutron form factors based on the dispersive approach applied directly to cross section data.

Acknowledgement

I am indebted to Yonghui Lin and Ulf-G. Meißner for their collaboration on the work presented in these proceedings. This work was supported by the Deutsche Forschungsgemeinschaft (DFG, German Research Foundation) – Projektnummer 279384907 – CRC 1245 and by the German Federal Ministry of Education and Research (BMBF) (Grant No. 05P24RDB).

References

[1] S. Pacetti, R. Baldini Ferroli and E. Tomasi-Gustafsson, *Proton electromagnetic form factors: Basic notions, present achievements and future perspectives*, *Phys. Rept.* **550-551** (2015) 1.

[2] V. Punjabi, C.F. Perdrisat, M.K. Jones, E.J. Brash and C.E. Carlson, *The Structure of the Nucleon: Elastic Electromagnetic Form Factors*, *Eur. Phys. J. A* **51** (2015) 79 [`1503.01452`].

[3] Y.-H. Lin, H.-W. Hammer and U.-G. Meißner, *Dispersion-theoretical analysis of the electromagnetic form factors of the nucleon: Past, present and future*, *Eur. Phys. J. A* **57** (2021) 255 [`2106.06357`].

[4] Y.-H. Lin, H.-W. Hammer and U.-G. Meißner, *Baryon Form Factors*, `2412.12885`.

[5] R. Pohl et al., *The size of the proton*, *Nature* **466** (2010) 213.

[6] A. Beyer et al., *The Rydberg constant and proton size from atomic hydrogen*, *Science* **358** (2017) 79.

[7] H. Fleurbaey, S. Galtier, S. Thomas, M. Bonnaud, L. Julien, F. Biraben et al., *New Measurement of the $1S-3S$ Transition Frequency of Hydrogen: Contribution to the Proton Charge Radius Puzzle*, *Phys. Rev. Lett.* **120** (2018) 183001 [`1801.08816`].

[8] N. Bezginov, T. Valdez, M. Horbatsch, A. Marsman, A.C. Vutha and E.A. Hessels, *A measurement of the atomic hydrogen Lamb shift and the proton charge radius*, *Science* **365** (2019) 1007.

[9] D.S. Armstrong and R.D. McKeown, *Parity-Violating Electron Scattering and the Electric and Magnetic Strange Form Factors of the Nucleon*, *Ann. Rev. Nucl. Part. Sci.* **62** (2012) 337 [`1207.5238`].

[10] F.E. Maas and K.D. Paschke, *Strange nucleon form-factors*, *Prog. Part. Nucl. Phys.* **95** (2017) 209.

[11] S. Bacca and S. Pastore, *Electromagnetic reactions on light nuclei*, *J. Phys. G* **41** (2014) 123002 [`1407.3490`].

[12] D.R. Phillips, *Electromagnetic Structure of Two- and Three-Nucleon Systems: An Effective Field Theory Description*, *Ann. Rev. Nucl. Part. Sci.* **66** (2016) 421.

[13] Y.-H. Lin, H.-W. Hammer and U.-G. Meißner, *New Insights into the Nucleon's Electromagnetic Structure*, *Phys. Rev. Lett.* **128** (2022) 052002 [`2109.12961`].

[14] S. Drell and F. Zachariasen, *Electromagnetic Structure of Nucleons*, Oxford University Press (1961).

[15] G. Höhler and E. Pietarinen, *Electromagnetic Radii of Nucleon and Pion*, *Phys. Lett. B* **53** (1975) 471.

[16] M. Hoferichter, B. Kubis, J. Ruiz de Elvira, H.-W. Hammer and U.-G. Meißner, *On the $\pi\pi$ continuum in the nucleon form factors and the proton radius puzzle*, *Eur. Phys. J. A* **52** (2016) 331 [`1609.06722`].

[17] W.R. Frazer and J.R. Fulco, *Effect of a pion pion scattering resonance on nucleon structure*, *Phys. Rev. Lett.* **2** (1959) 365.

[18] G. Höhler, *Pion-Nukleon-Streuung: Methoden und ergebnisse*, in *Landolt-Börnstein, 9b2*, H. Schopper, ed., (Berlin), Springer (1983).

[19] V. Bernard, N. Kaiser and U.-G. Meißner, *Nucleon electroweak form-factors: Analysis of their spectral functions*, *Nucl. Phys. A* **611** (1996) 429 [`hep-ph/9607428`].

[20] N. Kaiser and E. Passemar, *Spectral functions of nucleon form factors: Three-pion continua at low energies*, *Eur. Phys. J. A* **55** (2019) 16 [`1901.02865`].

[21] H.-W. Hammer and M.J. Ramsey-Musolf, *Spectral content of isoscalar nucleon form-factors*, *Phys. Rev. C* **60** (1999) 045205 [`hep-ph/9812261`].

[22] H.-W. Hammer and M.J. Ramsey-Musolf, *K anti-K continuum and isoscalar nucleon form-factors*, *Phys. Rev. C* **60** (1999) 045204 [`hep-ph/9903367`].

[23] U.-G. Meißner, V. Mull, J. Speth and J.W. van Orden, *Strange vector currents and the OZI rule*, *Phys. Lett. B* **408** (1997) 381 [`hep-ph/9701296`].

[24] M.A. Belushkin, H.-W. Hammer and U.-G. Meißner, *Dispersion analysis of the nucleon form-factors including meson continua*, *Phys. Rev. C* **75** (2007) 035202 [`hep-ph/0608337`].

[25] S. Kopecky, M. Krenn, P. Riehs, S. Steiner, J.A. Harvey, N.W. Hill et al., *Neutron charge radius determined from the energy dependence of the neutron transmission of liquid Pb-208 and Bi-209*, *Phys. Rev. C* **56** (1997) 2229.

[26] A.A. Filin, D. Möller, V. Baru, E. Epelbaum, H. Krebs and P. Reinert, *High-accuracy calculation of the deuteron charge and quadrupole form factors in chiral effective field theory*, *Phys. Rev. C* **103** (2021) 024313 [`2009.08911`].

[27] G.P. Lepage and S.J. Brodsky, *Exclusive Processes in Perturbative Quantum Chromodynamics*, *Phys. Rev. D* **22** (1980) 2157.

[28] S. Ciulli, C. Pomponiu and I. Sabba Stefanescu, *Analytic Extrapolation Techniques and Stability Problems in Dispersion Relation Theory*, *Acta Phys. Austriaca Suppl.* **14** (1975) 469.

[29] I. Sabba Stefanescu, *On the Stable Analytic Continuation With Rational Functions*, *J. Math. Phys.* **21** (1980) 175.

[30] P. Mergell, U.-G. Meißner and D. Drechsel, *Dispersion theoretical analysis of the nucleon electromagnetic form-factors*, *Nucl. Phys. A* **596** (1996) 367 [`hep-ph/9506375`].

[31] B. Efron and R. Tibshirani, *An introduction to the bootstrap*, *Statist. Sci.* **57** (1986) 54.

[32] S. Wesolowski, N. Klco, R.J. Furnstahl, D.R. Phillips and A. Thapaliya, *Bayesian parameter estimation for effective field theories*, *J. Phys. G* **43** (2016) 074001 [`1511.03618`].

[33] G. Höhler, E. Pietarinen, I. Sabba Stefanescu, F. Borkowski, G.G. Simon, V.H. Walther et al., *Analysis of Electromagnetic Nucleon Form-Factors*, *Nucl. Phys. B* **114** (1976) 505.

[34] I.T. Lorenz, U.-G. Meißner, H.-W. Hammer and Y.B. Dong, *Theoretical Constraints and Systematic Effects in the Determination of the Proton Form Factors*, *Phys. Rev. D* **91** (2015) 014023 [`1411.1704`].

[35] Y.-H. Lin, H.-W. Hammer and U.-G. Meißner, *High-precision determination of the electric and magnetic radius of the proton*, *Phys. Lett. B* **816** (2021) 136254 [`2102.11642`].

[36] J. Arrington, K. de Jager and C.F. Perdrisat, *Nucleon Form Factors: A Jefferson Lab Perspective*, *J. Phys. Conf. Ser.* **299** (2011) 012002 [`1102.2463`].

[37] A. Bianconi and E. Tomasi-Gustafsson, *Periodic interference structures in the timelike proton form factor*, *Phys. Rev. Lett.* **114** (2015) 232301 [`1503.02140`].

[38] R. Pohl, R. Gilman, G.A. Miller and K. Pachucki, *Muonic hydrogen and the proton radius puzzle*, *Ann. Rev. Nucl. Part. Sci.* **63** (2013) 175 [`1301.0905`].

[39] J.-P. Karr, D. Marchand and E. Voutier, *The proton size*, *Nature Rev. Phys.* **2** (2020) 601.

[40] H. Gao and M. Vanderhaeghen, *The proton charge radius*, *Rev. Mod. Phys.* **94** (2022) 015002 [`2105.00571`].

[41] A. Antognini et al., *Proton Structure from the Measurement of $2S-2P$ Transition Frequencies of Muonic Hydrogen*, *Science* **339** (2013) 417.

[42] P.J. Mohr, B.N. Taylor and D.B. Newell, *CODATA Recommended Values of the Fundamental Physical Constants: 2006*, *Rev. Mod. Phys.* **80** (2008) 633 [`0801.0028`].

[43] P. Mohr, D. Newell, B. Taylor and E. Tiesinga, *CODATA Recommended Values of the Fundamental Physical Constants: 2022*, `2409.03787`.

[44] A.C. Zemach, *Proton Structure and the Hyperfine Shift in Hydrogen*, *Phys. Rev.* **104** (1956) 1771.

[45] A1 collaboration, *High-precision determination of the electric and magnetic form factors of the proton*, *Phys. Rev. Lett.* **105** (2010) 242001 [`1007.5076`].

[46] D. Djukanovic, G. von Hippel, H.B. Meyer, K. Ottnad, M. Salg and H. Wittig, *Precision Calculation of the Electromagnetic Radii of the Proton and Neutron from Lattice QCD*, *Phys. Rev. Lett.* **132** (2024) 211901 [`2309.07491`].

[47] PACS collaboration, *Nucleon form factors in Nf=2+1 lattice QCD at the physical point: Finite lattice spacing effect on the root-mean-square radii*, *Phys. Rev. D* **109** (2024) 094505 [`2311.10345`].

[48] Y.-H. Lin, H.-W. Hammer and U.-G. Meißner, *The proton magnetic radius: A new puzzle?*, *Sci. Bull.* **69** (2024) 419 [`2312.08694`].

[49] MUSE collaboration, *The MUSE experiment*, *EPJ Web Conf.* **73** (2014) 07005.

[50] B. Adams et al., *Letter of Intent: A New QCD facility at the M2 beam line of the CERN SPS (COMPASS++/AMBER)*, `1808.00848`.